Supporting Information

Exchange Bias Effect in Ferro-/Antiferromagnetic van der Waals Heterostructures

Pawan Kumar Srivastava[1†], Yasir Hassan[2†], Hyobin Ahn[2], Byunggil Kang[2], Soon-Gil Jung[3,4], Yisehak Gebredingle[2], Minwoong Joe[1], Muhammad Sabbtain Abbas[4], Tuson Park[3,4], Je-Geun Park[5,6], Kyung-Jin Lee[7,8], Changgu Lee[1,2*]

[1]School of Mechanical Engineering, Sungkyunkwan University, Suwon, 16419, Republic of Korea.
[2]SKKU Advanced Institute of Nanotechnology (SAINT), Sungkyunkwan University, Suwon, 16419, Republic of Korea.
[3]Center for Quantum Materials and Superconductivity (CQMS), Sungkyunkwan University, Suwon, 16419, Republic of Korea.
[4]Department of Physics, Sungkyunkwan University, Suwon, 16419, Republic of Korea.
[5]Center for Correlated Electron Systems, Institute for Basic Science, Seoul, 08826, Republic of Korea.
[6]Department of Physics and Astronomy, Seoul National University, Seoul, 08826, Republic of Korea.
[7]Department of Materials Science and Engineering, Korea University, Seoul, 02841, Republic of Korea
[8]KU-KIST Graduate School of Converging Science and Technology, Korea University, Seoul, 02841, Republic of Korea.

Index.

S1. Methods

S2. Magnetization (M)-field (H) curve of bulk FGT at 2K.

S3. Exchange bias manipulation with field cooling in a FGT/CPS van der Waals FM/AFM heterojunction.

S4. Magnetic susceptibility *vs* temperature curves for various studied vdW AFM materials.

S5. Anomalous Hall measurement and field cooling effect on FGT/FPS based device.

S6. Brillouin-type temperature dependence of H_{EB} in FGT/CPS van der Waals FM/AFM heterojunction.

S7. Room temperature transfer characteristics of CPS based three-terminal field effect transistor.

S8. Room temperature transfer characteristics of FGT based three-terminal field effect transistor.

S9. Impact of semiconducting CPS layer on EB effect: Gate-dependent anomalous Hall measurements on FGT/CPS and only FGT based device.

S10. Atomic force microscopy/high resolution transmission electron microscopy/optical images of CPS and some of the measured FGT/CPS devices.

Table SI. Summary of FGT and CPS thicknesses in several measured devices.

S1. Methods.

Single crystal growth of Fe_3GeTe_2, $CrPS_4$, $FePS_3$, $NiPS_3$ and $MnPS_3$ Single crystal FGT was grown by the chemical vapor transport (CVT) method. High-purity Fe, Ge, and Te were mixed in powder form with molar proportions of 3:1:5 (Fe:Ge:Te). Iodine (5 mg/cm^2) was added as a transport agent and the mixed constituents were sealed into an evacuated quartz glass ampoule. This ampoule was placed in a tubular furnace, which has a temperature gradient between 650^{o}C and 700°C. Temperature of the central part of the furnace was ramped up to 700°C with a heating rate of 1°C per minute and was maintained at 700^{o}C for 96 h. To improve crystallinity of the flakes, the ampoule was slowly cooled down to 450 °C for over 250 h. Below 450 °C, the furnace was cooled rapidly to room temperature.

Single-crystalline $CrPS_4$ was also synthesized using CVT method. The mixture of powdered elements (99.5% Cr, 99.99% P, and 99.5% S with a molar ratio of 1:1:4; Sigma-Aldrich) was vacuum-sealed into a quartz ampule. This ampule was placed into a tubular furnace which has a temperature gradient, and the source side was in the high-temperature zone. The furnace temperature ramped to 700°C at the rate of 1°C/min and was kept at 700°C for 7 days. After that, the ampule was slowly cooled down to room temperature and broken in the ambient to collect the synthesized crystals.

Similar procedure as of $CrPS_4$ was followed for $FePS_3$, $NiPS_3$ and $MnPS_3$ synthesis with molar ratio of 1:1:3 for mixture of powdered elements (from Sigma Aldrich), Fe/Ni/Mn (99.5 %), P (99.99 %) and S (99.5 %), respectively.

Device fabrication and measurement. First, the single crystalline CPS was mechanically exfoliated and placed on a Si substrate with a 290 nm thickness SiO_2 layer. Then FGT flakes was mechanically exfoliated and transferred onto CPS flake using PDMS ((polydimethylsiloxane)) stamp. This exfoliation and stacking process was performed in a glovebox to prevent oxidation of the interface between the layers. Thickness of FGT and CPS flake was measured using atomic force microscope and HRTEM image of the cross section of heterostructures. Atomic force microscopic images yield monolayer thickness of ~ 1 nm. However, interlayer distance in CPS flakes as estimated via HRTEM was found to be 0.67 nm. Similarly, while for 2L, 3L and 8L CPS, thickness of 2 nm, 3 nm and 8 nm was extracted from atomic force microscopy, for same flakes, HRTEM images yielded 1.35 nm, 2.1 nm and 5.5 nm, respectively. Based on a correlation between such measurements, a calibration was used to estimate the number of layers in CPS (see Supporting Information section S9). Further, Hall bar geometry was patterned by e-beam lithography followed by Cr/Au (5 nm/80-100 nm) deposition. For electric field modulation of Hall signal, global back gate was applied through heavily doped silicon. During intervals between processing, the sample was covered with a Polymethylmethacrylate (PMMA) film and stored in a glove box with O_2:H_2O < 1 ppm. The sample was exposed to ambient for no more than 5 min throughout the fabrication procedure. After complete device fabrication process, active region of the device was covered with a thin hBN layer to protect it from ambient. Anomalous Hall measurements were performed in a low temperature cryostat (Cryomagnetics Inc, Oak Ridge, USA) equipped with maximum 9 T magnetic field. Signal was measured using SR830 lock-in amplifier and global gate was applied using Keithley 2400 source meter. Field cooling of the samples was performed in a variable temperature cryostat with cooling rate of ~5K/minute. The sample is cooled down well below T_N in the presence of a magnetic field (-1 T < B_{FC} < $+1$ T), and this situation is maintained for 30 minutes at the measurement temperatures. A first hysteresis loop is cycled to remove the training effect[1,2] and then a real measurement was taken. This process was repeated for magneto transport measurements on all samples.

HRTEM imaging. In first step, FM/AFM heterostructures on SiO_2/Si substrates were fabricated using standard procedure as mentioned above. Then focused ion beam milling was used to isolate a small portion of the heterojunction and then transferred to TEM grid for cross sectional HRTEM/STEM imaging. Acceleration voltage for TEM measurement was 200 keV. HRTEM images of cross section was used to measure thickness of respective flakes.

Computational details. In order to check the dependence of electron doping on magnetism of $CrPS_4$, we performed density functional theory (DFT) calculations with the projector augmented wave (PAW) method within generalized gradient approximation (GGA) developed by Perdew–Burke–Ernzerhof (PBE), as implemented in the Vienna *ab initio* simulation package (VASP). A plane wave basis sets with a kinetic energy cutoff of 500 eV was used. The *k*-points in the Brillouin zone were sampled using the Monkhorst-Pack scheme and chosen $2 \times 3 \times 2$ grids for the bulk $CrPS_4$ supercell. For geometry optimization, we used convergence criteria of 10^{-8} eV for the total energy in the electronic self-consistent loop, and 0.005 eV Å^{-1} for Hellmann–Feynman forces in the ionic relaxation loop. Taking the localized character of the 3*d* electrons of Cr into account, the rotationally invariant *GGA* + *U* scheme, proposed by Lie chtenstein *et al*,[3] was introduced with the values of Coulomb repulsion U = 3 eV and exchange coupling J = 1.4 eV. We included the van der Waals force for all of the calculations employing Grimme's method (DFT-D2) as implemented in VASP. Doping effect was simulated by modifying the total number of electrons per supercell as implemented in VASP, where homogeneous background charge is assumed. The total energy was obtained after structure optimization at each electron density.

S2. Magnetization (M)-field (H) curve of bulk FGT at 2K.

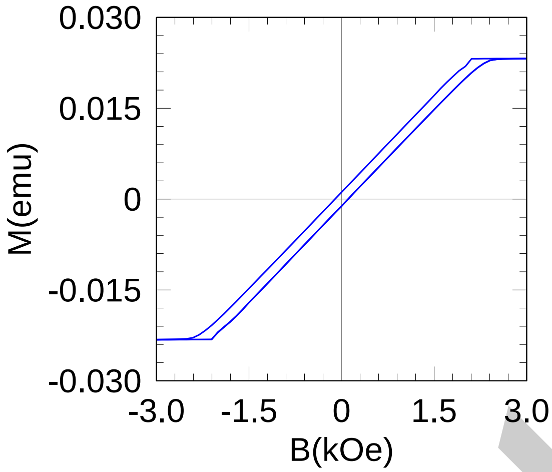

Fig. S1. Ferromagnetic M-H curve measured on bulk FGT flake in a physical property measurement system at T = 2K.

S3. Exchange bias manipulation with field cooling in a FGT/CPS van der Waals FM/AFM heterojunction.

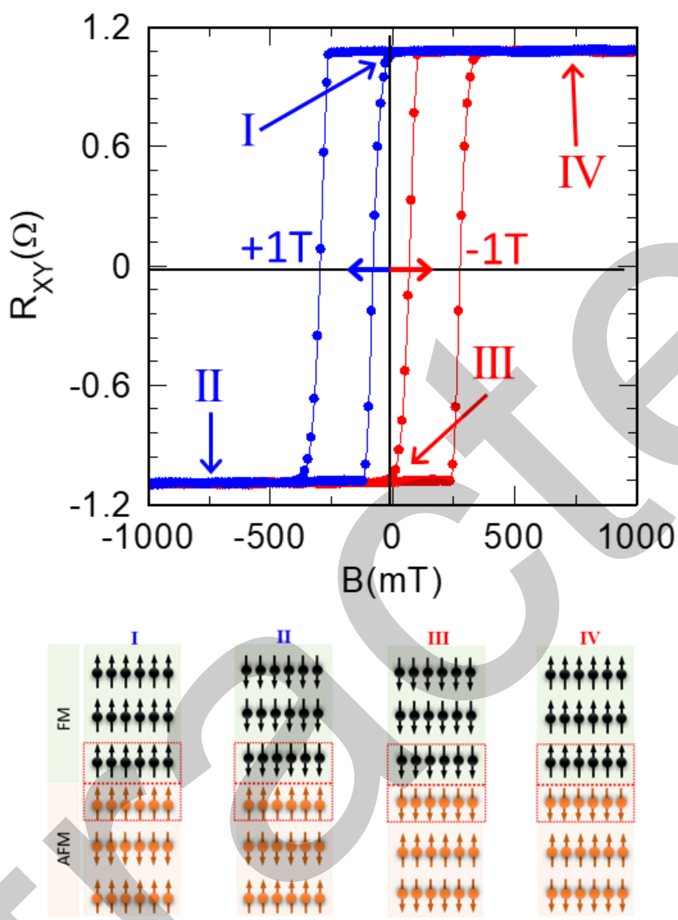

Fig. S2. Exchange bias in the FGT/CPS heterostructure probed by taking anomalous Hall measurements (excitation current = 1 mA). The polarity of the exchange bias field is manipulated by changing the polarity of the cooling field. An equivalent exchange bias field strength of ± 182 mT (indicated by double-headed arrows) can be achieved with a cooling field strength of ± 1 T. Schematic illustration of a spin flip mechanism at the FGT/CPS interface resulting from a sweeping magnetic field is also given. The various schematics (I-IV) in lower panel indicate spin orientations corresponding to those labeled in upper panel.

To demonstrate the ability to manipulate EB by using field cooling, we plotted hysteresis loops while changing the polarity and the set magnetic field during the field cooling process (Fig. S2). From this measurement, the exchange bias field (H_{EB}) was found to have almost identical shift of ~ 185 mT when the cooling field (B_{FC}) was varied in the range +1 T and -1 T. After field cooling ($T < T_B$), the initial FM configuration in FGT is imprinted on the AFM spin alignment in CPS if the cooling field is sufficiently strong to saturate the moments in the FM spin domains. Such imprinting is driven by the exchange interaction ($J_{FM\text{-}AFM}$) between moments of the FM and AFM that stimulates the moments in the AFM to align with those of the FM at the interface (Fig. S4c-I). At $T < T_B$, the moments in CPS remain pinned, irrespective of the direction of the sweeping magnetic field. Hence, the moments at the interface are oppositely aligned in FGT and CPS region when sweeping the polarity of magnetic field (Fig. S4c-II). When the coupling is induced between the two layers for $T < T_B$, the parallel configuration of the moments in the FGT and CPS is energetically more favored than the antiparallel configuration[4]. Consequently, the measured hysteresis loop is shifted on the magnetic field axis by a quantity termed as H_{EB} as discussed above. The behavior of the hysteresis loop shift and the opposite polarity of H_{EB} for field cooling with a -1 T set magnetic field can also be explained in a similar way (Fig. S2-II and III).

S4. Magnetic susceptibility *vs* temperature curves for various studied vdW AFM materials.

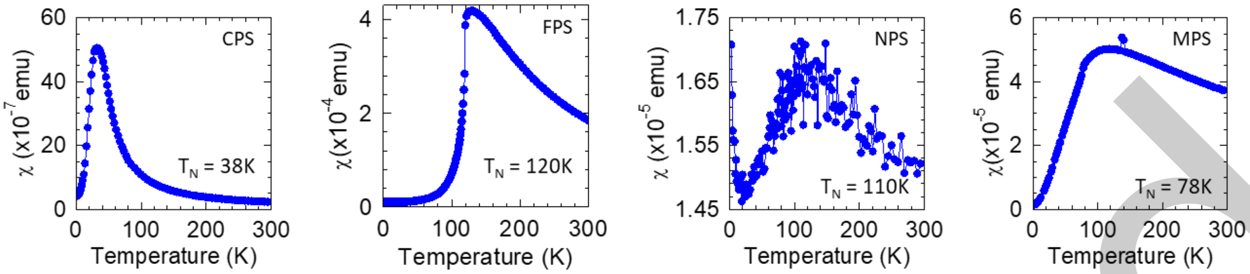

Fig. S3 Magnetic susceptibility (χ) vs temperature curves for CPS, FPS, NPS and MPS. Corresponding Néel temperatures (T_N) are extracted and labeled in respective Figs.

S5. Anomalous Hall measurement and field cooling effect on FGT/FPS based device.

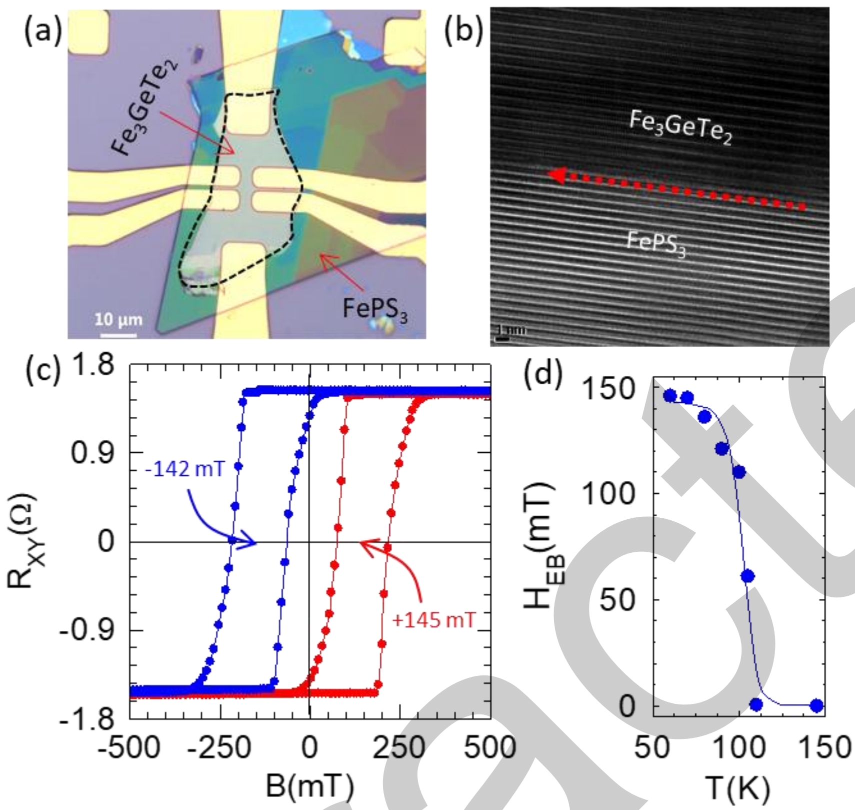

Fig. S4. (a) Optical image of FGT/FPS based Hall bar device (anomalous Hall data acquired on this device is given in Fig. 2b in main text). Dashed region indicates top FGT layer (30 nm). FPS flake (25 nm) is shown by an arrow. **(b)** HRTEM image of FGT/FPS interface acquired on the same device shown in A. **(c)** Exchange bias manipulation with field cooling in FGT/FPS van der Waals FM/AFM heterojunction. Exchange bias in FGT/FPS heterostructure probed by anomalous Hall measurement (excitation current = 5 mA). Polarity of the exchange bias field could be manipulated by changing the polarity of the cooling field (B_{FC}). Equivalent exchange bias field of ± 145 mT (indicated by arrows) can be achieved with cooling field of ± 1 T. We anticipate that similar out of plane spin orientation (Ising type) in both FGT (ref.[5,6]) and FPS (ref.[7]) favors the observation of EB effect in this vdW heterostructure. **(d)** Temperature dependent variation in H_{EB} extracted from Fig. 2b in main text. Exchange bias diminishes at T > 110K (shown by an arrow) known as blocking temperature (T_B) for FGT/FPS based EB device. Symbols are the data points and solid line is guide to eyes.

S6. Brillouin-type temperature dependence of H_{EB} in FGT/CPS van der Waals FM/AFM heterojunction.

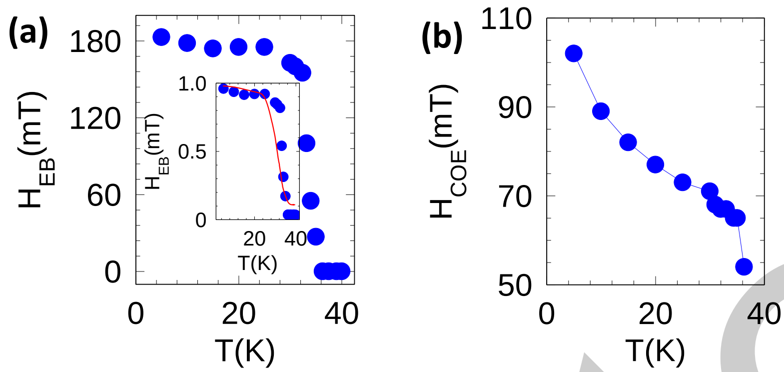

Fig. S5. (a) Plot of exchange bias field strength versus temperature, with the data for this plot extracted from data given in Fig. 2a in main text. The blocking temperature (~ 36.3 K) is indicated by an arrow. Inset shows the result of the data of a normalized version of this plot having been fit by the Brillouin function[8] expressed as $B_{B,T} = \frac{2J+1}{2J} coth\left(\frac{2J+1}{2J}\frac{g\mu_B JB}{k_B T}\right) - \frac{1}{2J} coth\left(\frac{1}{2J}\frac{g\mu_B JB}{k_B T}\right)$, where J the angular momentum (half integer or integer); μ_B the Bohr magneton, k_B the Boltzmann constant, and g the g-factor. For this fitting, we first normalized the data to have $H_{EB(max)}$ = 1 mT, then we considered J = 1/2, g-factor = 2 (pure spin), and B = +1 T (equivalent to the cooling field strength). Symbols are the data points and the solid line is the fit to the curve. **(b)** Plot of coercivity (H_{COE}) as a function of temperature, with the data for this plot extracted from data given in Fig. 2a in main text.

Assuming that a temperature-dependent AFM ordering is a primary source of the temperature-dependent change in H_{EB}, one can derive an expression for H_{EB} based on the simple consideration that reversing the FM moment in an FM-AFM EB system would require twice the energy of the exchange-coupled bonds across the FM-AFM interface. Balancing this energy with the Zeeman coupling leads to the following expression[9]

$$H_{EB} = \frac{2nJ_{FM-AFM}S_{FM}S_{AFM}}{a^2\mu_0 M_{FM}t_{FM}}, \qquad \text{(S-1)}$$

with a denoting the lattice parameter, n the number of uncompensated spins across the FM-AFM interface, $J_{FM\text{-}AFM}$ the exchange coupling constant, S_{FM} and S_{AFM} the spins of the FM and AFM materials, respectively, μ_o the vacuum permeability, and M_{FM} and t_{FM}, respectively, the magnetization and thickness of the FM layer. We fit the plot of H_{EB} versus temperature using equation S-1 and a couple of assumptions: one being that, since in our device the ordering temperature of CPS has been shown to be lower than that of FGT, the evolution of H_{EB} was mainly governed by a Brillouin-type temperature dependence of the AFM material; and the other assumption being that H_{EB} should be essentially zero at $T = T_N$. As shown in Fig. S5, the temperature dependence of H_{EB} was clearly reproduced using the Brillouin function. This reasonable fitting suggests that the temperature dependence of AFM ordering in CPS plays a dominant role in the evolution of H_{EB}. Note, however, that the fitting is not perfect (see the inset of Supporting Fig. S5a). We attribute the small deviations between the experimental H_{EB} and the fitting based on equation 1 to the EB phenomenon that is usually more complex than we assumed. The complexity of the EB effect is attributed to factors such as domain or domain wall formation in the AFM material, and dragging of AFM spins by FM spins[10]. For instance, the latter would cause a correlation between H_{EB} and H_{COE}, which was also partially observed in our sample (Figs. S5b): H_{COE} abruptly decreased as the temperature was increased in the vicinity of T_B (or T_N). A more detailed understanding of the EB effect in our vdW FM/AFM heterostructures requires further studies, which are beyond the scope of this work. Results and related discussions for Fig. S5 unambiguously support that the AFM ordering of CPS is the key to the EB effect observed in our samples.

S7. Room temperature transfer characteristics of CPS based three-terminal field effect transistor.

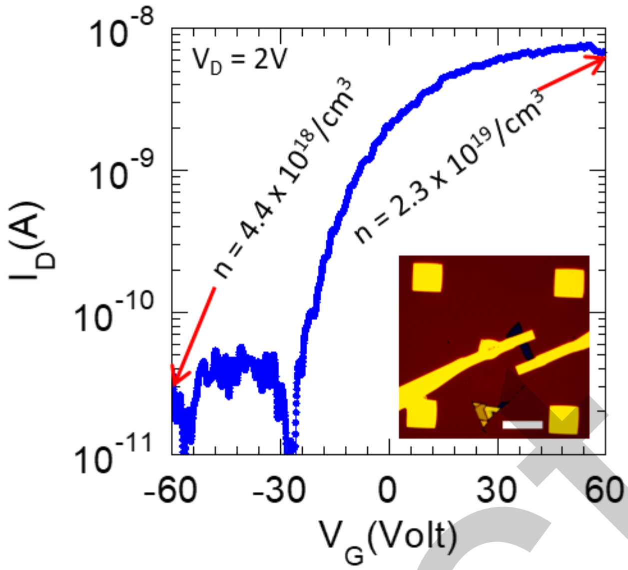

Fig. S6. Transfer characteristics (I_D-V_G) of three terminal CPS (20L) field effect device at fixed drain voltage, V_D = 2V (T = 300K). It is clear that CPS exhibits strong *n*-type semiconducting behavior. Optical image of measured device is given in inset. 2D carrier density (*n*) at a given gate voltage was calculated using expression $n = \frac{C_g(V_G - V_{th})}{e}$ where Cg, the gate capacitance (10.1 nF for 290 nm thick SiO_2 dielectric); V_{th}, the threshold voltage ~ -30V and *e*, the electronic charge. Inset shows the optical image of the measured device. Scale bar: 10 µm. CPS is a semiconductor with energy band-gap of ~ 1.3 eV, and similar n-type conduction in CPS has been observed before[11]. Field effect transistors (on SiO_2 dielectric) based on thin CPS (< 5L-10L) show no conductivity and gate modulation. Hence, to observe the substantial carrier modulation through gate, sufficiently thick CPS is required (also *see* ref.[8]).

S8. Room temperature transfer characteristics of FGT based three-terminal field effect transistor.

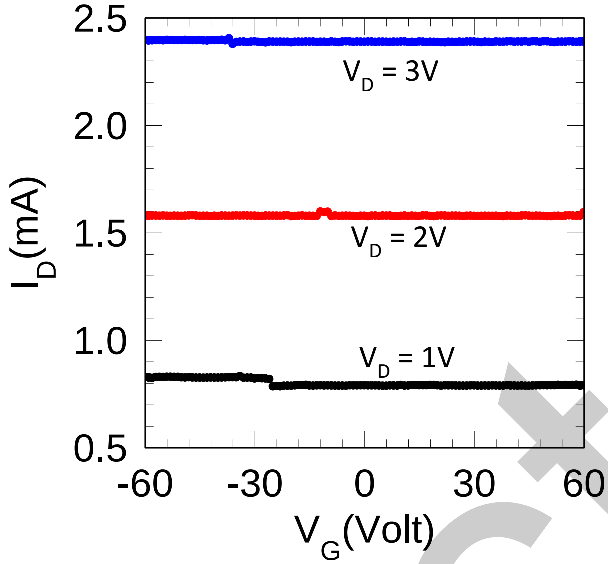

Fig. S7. Transfer characteristics (I_D-V_G) of three terminal FGT (25 nm thick) field effect device at fixed drain voltages, V_D = 1V, 2V and 3V as labelled (T = 300K). Negligible gate dependence indicates metallic behavior of FGT flake as reported earlier[6,12].

S9. Impact of semiconducting CPS layer on EB effect: Gate-dependent anomalous Hall measurements on FGT/CPS and only FGT based device.

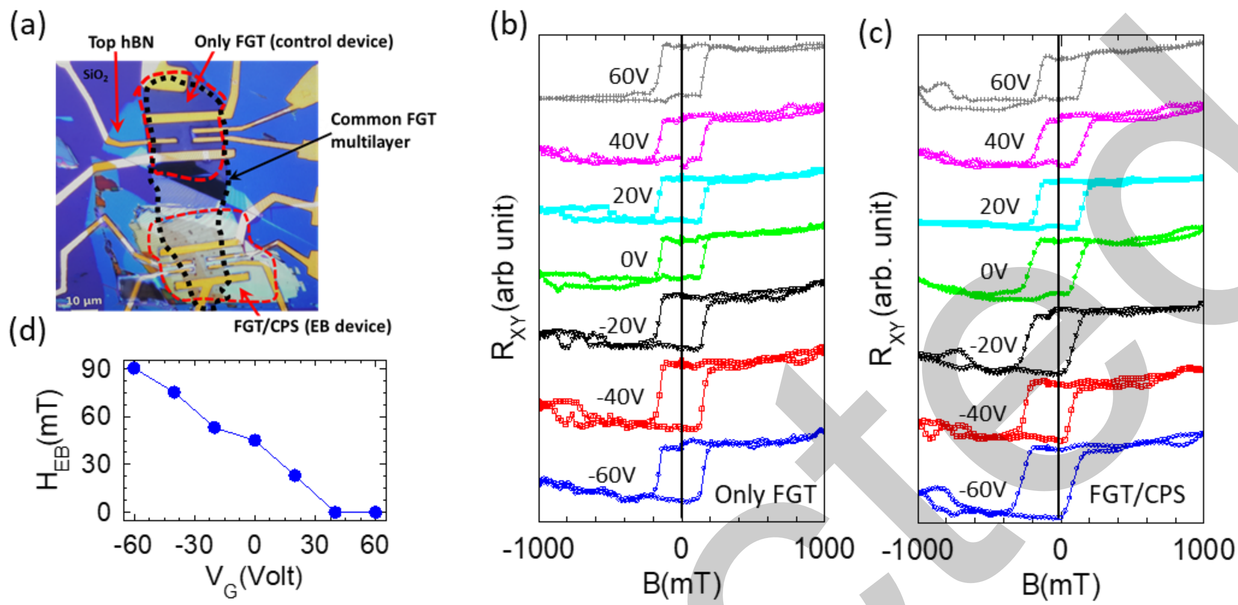

Fig. S8. (a) Optical image of Hall bar device (on SiO_2/Si (n^{++}) substrate) which has two segments with (*i*) only FGT (control device) and (*ii*) FGT (top)/CPS (bottom) as EB device. These devices share the same FGT flake (shown by black dot region). The thicknesses of FGT and CPS are 14 nm and 35 nm, respectively. Active area of the device was covered by top-hBN flake. **(b)** Hysteresis in R_{XY} vs magnetic field at different gate voltages in only FGT based Hall bar device. **(c)** Hysteresis in R_{XY} vs magnetic field at different gate voltages in FGT/CPS based Hall bar device (excitation current = 1mA). Cooling field for these measurements was fixed at +1 T. **(d)** Gate-dependent exchange bias field (H_{EB}) extracted from D. It can be clearly seen that no horizontal shift in hysteresis was observed for bare FGT based Hall bar device shown in C. However, horizontal shift in hysteresis curve and substantial V_G dependence has been observed for FGT/CPS based Hall bar device (c and d), illustrating the importance of bottom CPS layer for the observation of EB effect as discussed in main text. Horizontal shift in hysteresis curve is an indication of EB effect[10,13].

As discussed in Supporting section S6, back gate modulation of carriers in CPS requires a critical thickness. Thickness dependent evolution of exchange bias field also works in similar way *i.e*. exchange bias field initially increases and then plateaued with increase of CPS thickness. We have been able to measure the devices with maximum $CrPS_4$ thickness up to 35 layers and details are already provided in Supporting section S9 and Table S1. In this view, effective exchange bias and its gate voltage tunability, both could be achieved simultaneously in devices with sufficiently thick CPS.

S10. Atomic force microscopy/high resolution transmission electron microscopy/optical images of CPS and some of the measured FGT/CPS devices.

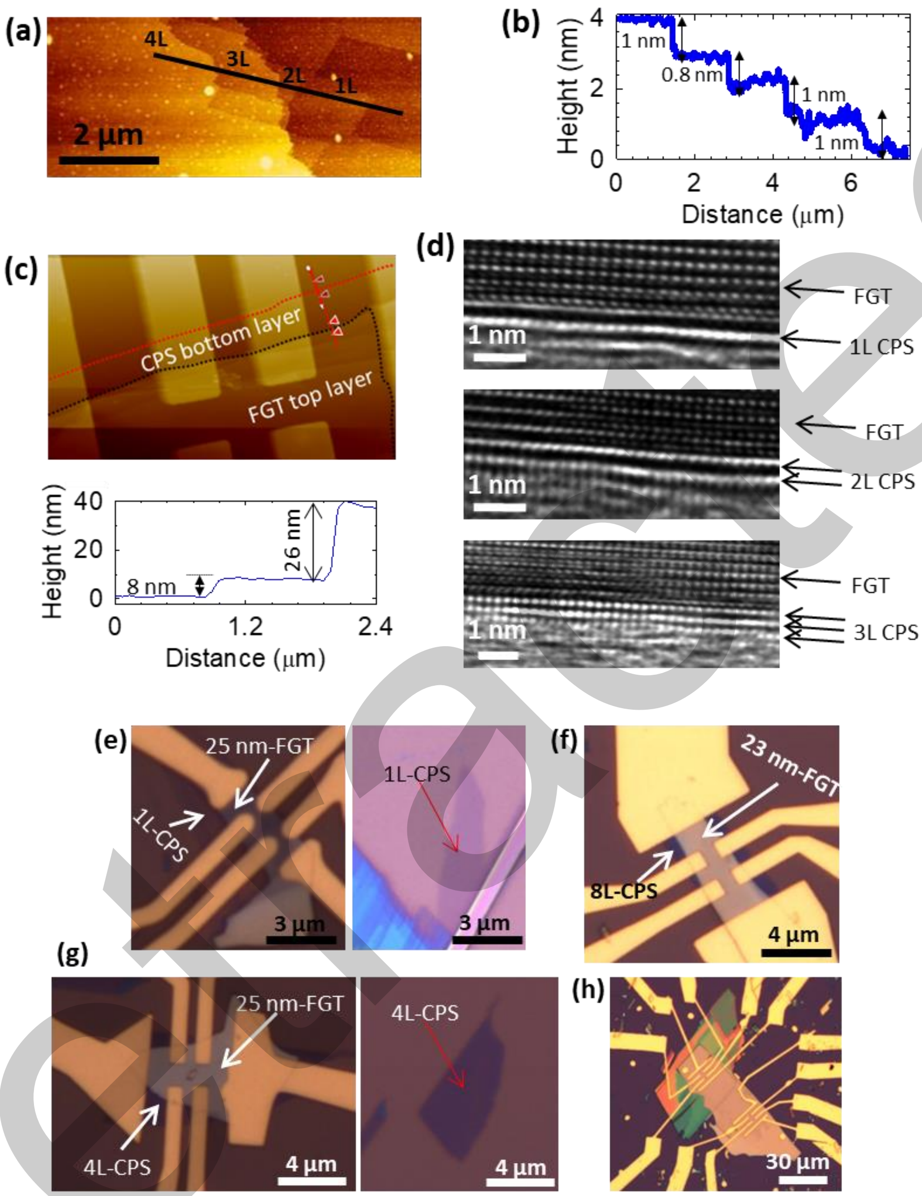

Fig. S9. (a) Atomic force microscopy (AFM) image of CPS layers. **(b)** Height profile along the solid line in (a) yields monolayer thickness of 1 nm as indicated by arrows. **(c)** AFM image of a heterostructure device with 8 nm CPS (8L) and 26 nm FGT. **(d)** High resolution transmission electron microscopic (HRTEM) image of cross section of FGT/ CPS heterostructures. Top FGT and bottom CPS layers have been indicated by arrows. In contrast to AFM, HRTEM image yielded interlayer distance of 0.7 nm in CPS. This correlation between thickness obtained using AFM and HRTEM was used to identify number of CPS layers in various FGT/ CPS heterostructures. **(e-h)** Optical images of some of the measured FGT/CPS devices with varying CPS thickness. In (e) and (g) optical image of 1L and 4L CPS before device fabrication is also given.

Table-S1. Summary of FGT and CPS thicknesses and exchange bias field (H_{EB}) in several measured devices. Thicknesses of FGT and CPS were duly confirmed *via* atomic force microscopy and high resolution transmission electron microscopic image of cross sections of measured devices (see methods section).

FGT thickness (nm)	CPS (No. of atomic layers)	H_{EB} (mT)
10	01	0
10	02	10 ± 4
10	03	16
23	04	28
25	16 ± 02	135 ± 10
25	55	167
26	08	67
28	01	0
30	20 ± 02	180 ± 12
35	35 ± 03	193 ± 15

Supporting references.

(1) Salabaş, E. L.; Rumplecker, A.; Kleitz, F.; Radu, F.; Schuth, F. Exchange Anisotropy in Nanocasted Co_3O_4 Nanowires. *Nano Lett.* **2006**, *6* (12), 2977–2981.

(2) Hauet, T.; Borchers, J. A.; Mangin, P.; Henry, Y.; Mangin, S. Training Effect in an Exchange Bias System: The Role of Interfacial Domain Walls. *Phys. Rev. Lett.* **2006**, *96* , 067207.

(3) Liechtenstein, A. I.; Anisimov, V. I.; Zaanen, J.; Density-functional theory and strong interactions: Orbital ordering in Mott-Hubbard insulators. *Phys. Rev.* **1995**, *52* (8), 5467–5471.

(4) Jungwirth, T.; Marti, X.; Wadley, P.; Wunderlich, J. Antiferromagnetic Spintronics. *Nat. Nanotechnol.* **2016**, *11* (3), 231–241.

(5) Tan, C.; Lee, J.; Jung, S. G.; Park, T.; Albarakati, S.; Partridge, J.; Field, M. R.; McCulloch, D. G.; Wang, L.; Lee, C. Hard Magnetic Properties in Nanoflake van Der Waals Fe_3GeTe_2. *Nat. Commun.* **2018**, *9* (1), 1554.

(6) Deng, Y.; Yu, Y.; Song, Y.; Zhang, J.; Wang, N. Z.; Sun, Z.; Yi, Y.; Wu, Y. Z.; Wu, S.; Zhu, J.; et al. Gate-Tunable Room-Temperature Ferromagnetism in Two-Dimensional Fe_3GeTe_2. *Nature* **2018**, *563* (7729), 94–99.

(7) Lee, J. U.; Lee, S.; Ryoo, J. H.; Kang, S.; Kim, T. Y.; Kim, P.; Park, C. H.; Park, J. G.; Cheong, H. Ising-Type Magnetic Ordering in Atomically Thin $FePS_3$. *Nano Lett.* **2016**, *16* (12), 7433–7438.

(8) Sepioni, M.; Nair, R. R.; Rablen, S.; Narayanan, J.; Tuna, F.; Winpenny, R.; Geim, A. K.; Grigorieva, I. V. Limits on Intrinsic Magnetism in Graphene. *Phys. Rev. Lett.* **2010**, *105* (20), 207205.

(9) Van der Zaag, P. J.; Ijiri, Y.; Borchers, J. A.; Feiner, L. F.; Wolf, R. M.; Gaines, J. M.; Erwin, R. W.; Verheijen, M. A. Difference between Blocking and Néel Temperatures in the Exchange Biased Fe_3O_4/CoO system. *Phys. Rev. Lett.* **2000**, *84* (26), 6102–6105..

(10) Schuller, I. K.; Nogués, J. Exchange Bias. *J. Magn. Magn. Mater.* **1999**, *192*, 203–232.

(11) Lee, J.; Ko, T. Y.; Kim, J. H.; Bark, H.; Kang, B.; Jung, S. G.; Park, T.; Lee, Z.; Ryu, S.; Lee, C. Structural and Optical Properties of Single- and Few-Layer Magnetic Semiconductor $CrPS_4$. *ACS Nano* **2017**, *11* (11), 10935–10944.

(12) Luo, L.; Lai, X.; Feng, W.; Zhang, Y.; Zhu, X.; Tan, S.; Liu, Y.; Zhang, Z.; Chen, Q.; Liu, Q.; *et al*. Emergence of Kondo Lattice Behavior in a van Der Waals Itinerant Ferromagnet, Fe_3GeTe_2 . *Sci. Adv.* **2018**, *4* (1), eaao6791.

(13) Wu, S. M.; Cybart, S. A.; Yu, P.; Rossell, M. D.; Zhang, J. X.; Ramesh, R.; Dynes, R. C. Reversible Electric Control of Exchange Bias in a Multiferroic Field-Effect Device. *Nat. Mater.* **2010**, *9* (9), 756–761.